Jitendra P. Khatait[1]
Mechanical Automation and Mechatronics,
Faculty of Engineering Technology,
University of Twente,
7500 AE Enschede, The Netherlands
e-mail: j.p.khatait@utwente.nl

Dannis M. Brouwer
Mechanical Automation and Mechatronics,
Faculty of Engineering Technology,
University of Twente,
7500 AE Enschede, The Netherlands;
Demcon Advanced Mechatronics,
7521 PH Enschede, The Netherlands

Herman M. J. R. Soemers
Philips Innovation Services,
5656 AE Eindhoven, The Netherlands

Ronald G. K. M. Aarts

Just L. Herder

Mechanical Automation and Mechatronics,
Faculty of Engineering Technology,
University of Twente,
7500 AE Enschede, The Netherlands

Design of an Experimental Set-Up to Study the Behavior of a Flexible Surgical Instrument Inside an Endoscope

The success of flexible instruments in surgery requires high motion and force fidelity and controllability of the tip. However, the friction and the limited stiffness of such instruments limit the motion and force transmission of the instrument. In a previous study, we developed a flexible multibody model of a surgical instrument inside an endoscope in order to study the effect of the friction, bending and rotational stiffness of the instrument and clearance on the motion hysteresis and the force transmission. In this paper, we present the design and evaluation of an experimental setup for the validation of the flexible multibody model and the characterization of the instruments. A modular design was conceived based on three key functionalities: the actuation from the proximal end, the displacement measurement of the distal end, and the measurement of the interaction force. The exactly constrained actuation module achieves independent translation and rotation of the proximal end. The axial displacement and the rotation of the distal end are measured contactless via a specifically designed air bearing guided cam through laser displacement sensors. The errors in the static measurement are 15 μm in translation and 0.15 deg in rotation. Six 1-DOF load cell modules using flexures measure the interaction forces and moments with an error of 0.8% and 2.5%, respectively. The achieved specifications allow for the measurement of the characteristic behavior of the instrument inside a curved rigid tube and the validation of the flexible multibody model.
[DOI: 10.1115/1.4024660]

Keywords: experimental setup, design, evaluation, flexible wire, surgical instrument

1 Introduction

Surgical robotic systems have overcome many of the limitations of conventional laparoscopic systems by increasing dexterity, restoring proper hand-eye coordination and an ergonomic working position, and improving visualization [1–3]. The surgical robotic systems often employ rigid instruments to perform surgical procedures. However, the use of rigid instruments limits the reach and accessibility to the diseased tissues or organs.

Furthermore, flexible surgical instruments are increasingly incorporated to perform therapeutic procedures during conventional flexible endoscopy. The emergence of natural orifice transluminal endoscopic surgery (NOTES) and single incision laparoscopic surgery (SILS) procedures necessitates the use of flexible endoscopy in performing more invasive procedures [4,5]. In such interventions, a surgical instrument is fed through an access channel provided in the endoscope or endoscopic platform. Figure 1 shows a typical flexible endoscope with a surgical instrument used for colonoscopy [6]. The surgical instrument has limited stiffness so that it can be easily inserted through the endoscope. The motion and force are transmitted to the distal end of the instrument by actuating the proximal end. However, the friction and the limited stiffness of the instrument limit the motion and force fidelity of the instrument. Precise control of these instruments inside the body is critical for achieving successful surgical outcomes.

Modeling and simulation techniques help in developing better insight into the dynamic behavior of a flexible instrument inside an endoscope. This offers an improved design of the instrument and the controller and eventually leads to the improved motion and force fidelity of the instrument. In our previous studies [7–9], we described the flexible multibody model to study the dynamic behavior of a flexible surgical instrument inside an endoscope. We studied the effect of the friction, bending and rotational stiffness of the instrument, and clearance on motion hysteresis. The simulation results showed stick-slip behavior and motion hysteresis. We designed an experimental setup to validate the model and simulation results.

The design and evaluation of the setup is discussed in this paper. The design objective is introduced along with the design requirements and the specifications in Sec. 2. The details of the design of the experimental setup and its evaluation are described in Secs. 3 and 4, respectively. Section 5 discusses the design evaluation. The conclusion is presented in Sec. 6.

2 Design Objective

The design specifications were chosen with respect to a typical surgical scenario—with a flexible instrument inside an endoscope—where the surgeon controls the instrument from its proximal end. The endoscope provides a rigid support to the instrument. The placement and the orientation of the instrument tip are essential to safely perform the surgical procedure. The instrument tip can carry different surgical tools to perform different procedures. The force delivered at the tip is critical for the successful operation and the safety of the patient as well. During the surgical procedure, the interaction forces will be applied on the endoscope by the instrument and vice versa. The friction between the instrument and the endoscope limits the motion and force

[1]Corresponding author.

Manuscript received May 29, 2012; final manuscript received April 11, 2013; published online July 3, 2013. Assoc. Editor: Carl A. Nelson.

Fig. 1 Endoscope with surgical instrument [6]

delivery at the tip. At the same time it also results in nonlinear dynamic behavior such as stick-slip and motion hysteresis.

The design objectives of the setup are, therefore, as follows:

(1) to manipulate the instrument tip from the proximal end
(2) to measure the motion of the instrument tip
(3) to measure the force of interaction between the instrument and the endoscope

The setup will be used for validation experiments. Since the endoscope is rather stiff as compared to the instrument and is also well supported inside the body cavity by the adjacent organs, the endoscope is modeled as a curved rigid tube. The experiments will also be performed using a curved rigid tube. Moreover, the setup should be able to accommodate different configurations of the rigid tube. It can be further extended to include different kinds of loading at the tip.

2.1 Design Requirements. The instrument is manually inserted inside the tube until the distal end is out of the tube. The proximal and distal ends are attached to the respective modules for the actuation and measurement, respectively. The tube is rigidly fixed on a platform which measures the force of interaction between the instrument and the tube.

The instrument is manipulated both in translation and rotation to perform a surgical procedure. The surgeon gets the visual feedback of the operation. The required resolution [10,11] is of the order of 0.1 mm in translation and 1 deg in rotation. The range of motion is ± 20 mm in translation and ± 2 revolutions. The maximum speed can be 20–50 mm/s in translation and 5–10 rev/s in rotation. However, the friction induced nonlinear dynamic behavior is more prominent at near zero speed. Therefore, the instrument should be able to move at low speed; for example, 0.2 mm/s. Both the rotation and translation can be independently varied so that we can obtain a combination of motions.

The force delivery at the tip can be on the order of 5–10 N with a resolution of 0.01 N [12,13]. The force transmission at the tip is critical for tissue manipulation and for performing surgical procedures such as needle steering, suturing, cutting, etc. Essentially, the tip should be able to deliver force and torque in the longitudinal direction.

The displacement measurement of the distal end of the instrument can provide vital information about the instrument's characteristic behavior. The motion hysteresis and stick-slip behavior can be quantified by measuring and comparing the tip motion with the input motion. The range and resolution of motion at the output are of the same order as the actuation side. Moreover, during the stick-slip motion, the instrument tip can suddenly be released and, therefore, the required bandwidth for measuring the motion at the tip will be higher than at the proximal end.

When the instrument is manipulated inside the tube, a force is exerted on the instrument by the tube because of friction, the convoluted shape of the tube, and the stiffness of the instrument. The measurement of this interaction force is required in order to study the effect of various parameters on the force of interaction. The range and resolution of the force measurement can be of the order of the force required at the tip for various surgical procedures.

Apart from these technical requirements, the setup should also be able to cater to other requirements. Tubes of different shapes and sizes should be easily mounted. The setup should be robust and safety features should be included to safeguard the sensors and other critical components. The displacement measurement of the tip of the instrument with the contact sensors and components can alter the behavior of the instrument. Therefore, contactless measurement is preferred for the displacement measurement at the tip.

2.2 Design Specifications. A modular design was sought for the setup since this would enable easy reconfiguration for future experiments. The experimental setup, therefore, consists of three basic modules (see Fig. 2):

(1) actuation module (AM)
(2) force sensing module (FSM)
(3) tip motion measurement module (T3M)

The AM provides necessary actuation along each degree-of-freedom (DOF) required at the proximal end of the instrument, i.e., translation and rotation along the longitudinal axis of the instrument. The AM can be aligned along the entry of the tube and the proximal end of the instrument can be attached to the AM for the actuation.

The FSM enables the measurement of forces and torques arising from the interaction of the instrument with the guide tube. A guide tube of different geometric configurations can be rigidly attached on the top plate of the FSM. Load cells can be embedded to measure the forces and torques in all directions.

The T3M measures the translation and rotation of the distal end of the instrument along the longitudinal axis. The T3M can be aligned along the exit of the guide tube and the distal end of the instrument can be attached to the T3M for the displacement measurement.

Based on the design requirements, the design specifications of the three modules—AM, FSM, and T3M—are summarized in Table. 1. The resolution of motion required for the setup is better than what is required by the surgeon or the surgical procedure since the setup is intended for the characterization and model validation of the instrument. The achieved specifications, which will be discussed later in Sec. 4, are also summarized in the table for comparison.

3 Design of the Experimental Setup

The conceptual design and the design embodiment of the AM, FSM, and T3M are described in detail in the following sections. The experimental setup also includes the real-time measurement system. The software and hardware are also discussed.

3.1 Design of the AM. The AM consists of actuation in 2-DOFs—translation and rotation along the longitudinal axis of the

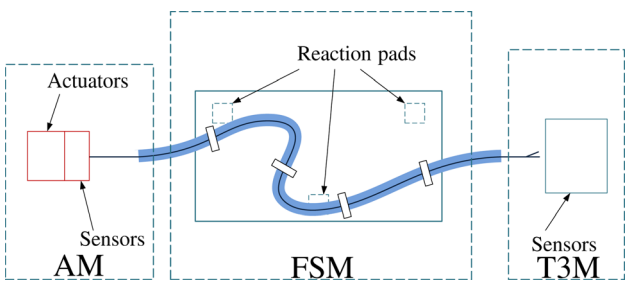

Fig. 2 Schematic drawing of the experimental setup

Table 1 Specifications of the set-up

	Description	Specifications	
		Design	Achieved
AM	Translation		
	Range (mm)	50	50
	Resolution (μm)	10	0.1[a]
	Speed (mm/s)	0–10	0–30[b]
	Error (mm)	0.1	0.2[c]
	Rotation		
	Range (revolutions)	± 5	unlimited
	Resolution (deg)	0.01	0.005[a]
	Speed (rev/s)	0–5	0–4[b]
	Error (deg)	0.1	1.0[c]
T3M	Translation		
	Range (mm)	50	50
	Resolution (μm)	10	15[d]
	Speed (mm/s)	0–10	0–30
	Error (mm)	0.1	0.01
	Rotation		
	Range (revolutions)	± 5	unlimited
	Resolution (deg)	0.01	0.15[d]
	Speed (rev/s)	0–5	0–4
	Error (deg)	0.1	1.0
FSM	Forces in the *xyz*-direction		
	Range (N)	±50	±50
	Resolution (N)	0.010	0.009[d]
	Error (%)	1.0	0.8
	Torque in the *xyz*-direction		
	Range (Nm)	± 0.2	± 8.0
	Resolution (Nm)	0.002	0.0015[d]
	Error (%)	1.0	2.5

[a]Based on encoder resolution.
[b]Based on motor speed.
[c]Due to gear backlash.
[d]For a cut-off frequency of 45 Hz.

instrument. We wanted to have independent actuation for both DOFs; therefore, we chose a stacked configuration. Translation is achieved through a ball screw. A preloaded ball screw nut is used to avoid backlash. However, this adds additional friction in the drive. The motor encoder is used to measure the translation of the AM.

The rotation axis is mounted on a linear slide guide. The assembly of the ball screw and the slide guide requires the alignment of the two axes. If rigidly connected, any misalignment causes an increase in the frictional force and deteriorates the repeatability of the setup. For long stroke motion, the misalignment can even lead to jamming of the stage. Following the principles of an exactly constrained design using flexures [14], a coupling is designed to connect the ball screw nut to the slide guide. An exactly constrained design leads to smaller internal forces due to misalignment and, therefore, it relaxes the alignment requirements—reducing the total effort and cost—during the assembly [10,14,15].

3.1.1 Design of the Exactly Constrained Coupling. The coupling has to be stiff in the translation and the rotation direction along the translation axis. The ball screw nut should be constrained in rotation so that the rotary motion of the ball screw is converted into the linear motion of the nut. The linear displacement of the nut x is related to the rotation of the ball screw n through the pitch of the ball screw p as ($x = pn$). A constraint in translation along the same axis transfers the linear motion of the nut to the slide guide. The coupling is compliant in the other 4-DOFs.

An exactly constrained coupling is designed using a bellow flexure and a folded sheet flexure. Figure 3 shows the conceptual

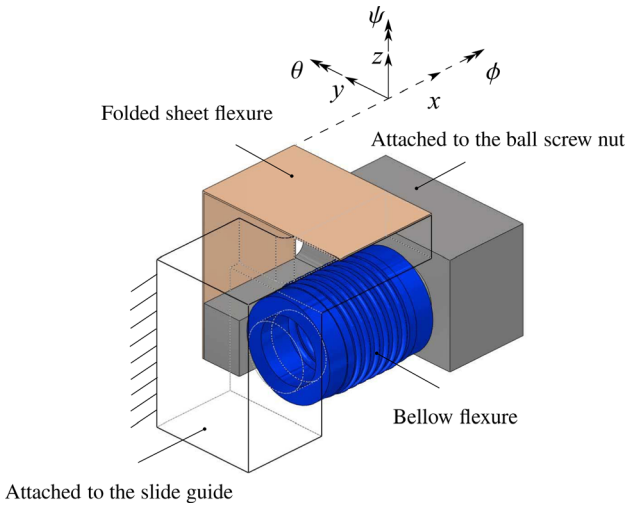

Fig. 3 Conceptual design of the coupling for the ball screw and slide guide using a folded sheet flexure and a bellow flexure. The stiff directions are shown by the dashed arrows. The compliant directions are shown by the solid arrows.

design of the coupling. A folded sheet flexure [14–16] constrains the two ends, parallel to the axis of the fold, only along the axis of the fold. All other 5-DOFs are compliant. Therefore, it can accurately transfer the linear motion from one side to the other. Any misalignment can be easily accommodated by the flexure. Likewise, a bellow flexure can constrain the two sides in rotation along the axis of bellow. It is compliant in the other 5-DOFs. The two flexures should be connected in parallel to provide constraints in exactly the 2-DOFs as shown in Fig. 3.

The stiffness of the folded sheet flexure along the folding line for equally long sides (with length l) is given by [14]

$$k = \left[2\left(\frac{l^3}{3EI} + \frac{6}{5}\frac{l}{GA}\right)\right]^{-1} \quad (1)$$

where A is the cross-section area, I is the area moment of inertia, E is Young's modulus of elasticity, and G is the shear modulus of the folded sheet flexure. The stiffness value should be such that the friction force in the translation direction should not significantly affect the positional accuracy. Table 2 shows the specifications of the folded sheet flexure. Similarly, the bellow flexure is selected for high rotational stiffness. The rotational stiffness of the bellow flexure should be able to provide the reaction torque arising due to the friction between the ball screw and the nut without significantly affecting the accuracy. The specifications are shown in Table 2.

The flexure coupling should tolerate misalignment because of the inclination and offset distance between the ball screw and the slide guide. The maximum misalignment can be tolerated by the flexure coupling as the DOFs in those directions are released and the coupling is compliant in those directions. The allowable offset and inclination for the bellow flexure appears to be rather small

Table 2 Specifications of the flexure coupling

Description	Specifications
Folded sheet flexure	
Stiffness (N/m)	1.66×10^6
Allowable offset (mm)	2
Bellow flexure	
Torsional stiffness (Nm/rad)	220
Allowable offset (mm)	0.15
Allowable inclination (deg)	2

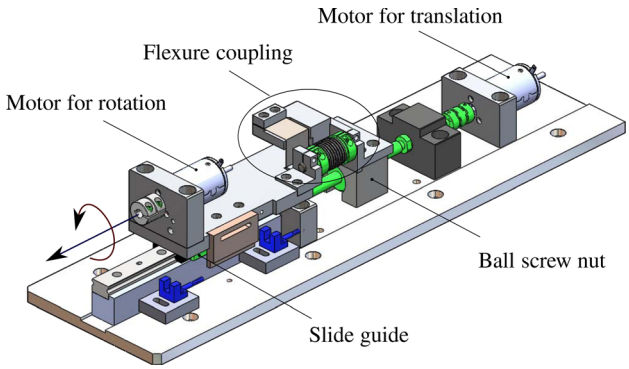

Fig. 4 Conceptual design of the AM. The translation and rotation axis is connected via a flexure coupling. The two actuated DOFs are shown by the arrows.

since it is designed for a longer fatigue life [17]. This is a very conservative value for the intended application since it is for non-fatigue use. An offset of about 10 times the specified value can be easily achieved.

3.1.2 Design Embodiment of the AM. A precision ball screw and slide guide were selected [17]. We chose two DC motors for actuating both DOFs [18]. The folded sheet flexure was made out of a stainless steel sheet 0.3 mm in thickness, 20 mm in width, and 30 mm in length for each side. The bellow flexure was selected and purchased off-the-shelf [17]. Figure 4 shows the conceptual design of the AM. The AM included a gear box for the actuation in each DOF. The gear box helped in achieving the lower speed. It also reduced the motor torque initially required to move the AM.

3.2 Design of the FSM. The FSM was designed to measure the forces arising from the interaction between the instrument and the guide tube. The force measurements along six DOFs are required to measure all of the possible components of the resultant force. A combination of 1-DOF load cells and *n*-DOFs load cells can be used in various configurations to obtain a total 6-DOFs force measurement. We chose six 1-DOF load cells and used the exactly constrained design principles [10,14,15] to design the FSM.

The size of the FSM was chosen so that a curved tube, on the order of human anatomical features, can be accommodated and can be configured easily. Moreover, for the purpose of model validation, the curvature of the tube can be relaxed and, therefore, a curved tube of larger dimensions should also be accommodated and can be attached.

3.2.1 Exactly Constrained Configuration of the FSM. The conceptual design of an exactly constrained configuration of the FSM using six wire flexures is shown in Fig. 5. A wire flexure constrains only one DOF, i.e., along the longitudinal direction. It is compliant in the other five DOFs. Three wire flexures were placed underneath the floating platform along the *z*-axis, constraining three DOFs–translation along the *z*-axis and two rotations along the *x*- and *y*-axis. Two wire flexures were placed along the *x*-axis, constraining the other two DOFs—translation along the *x*-axis and rotation along the *z*-axis. One wire flexure was placed along the *y*-axis, constraining the translation along the *y*-axis. Consequently, the floating top platform was fully constrained by the six wire flexures.

The force vector $\mathbf{F}_x$, acting at the center of the top plate of the FSM, can be transformed into another force vector $\mathbf{F}_n$ as

$$\mathbf{F}_x = A\mathbf{F}_n$$

or

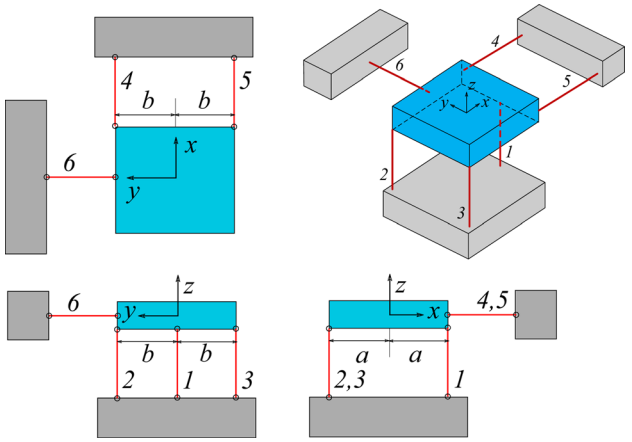

Fig. 5 Conceptual design of an exactly constrained configuration of the FSM using six wire flexures

$$\begin{bmatrix} F_x \\ F_y \\ F_z \\ M_x \\ M_y \\ M_z \end{bmatrix} = \begin{bmatrix} 0 & 0 & 0 & -1 & -1 & 0 \\ 0 & 0 & 0 & 0 & 0 & -1 \\ 1 & 1 & 1 & 0 & 0 & 0 \\ 0 & b & -b & 0 & 0 & 0 \\ -a & a & a & 0 & 0 & 0 \\ 0 & 0 & 0 & b & -b & 0 \end{bmatrix} \begin{bmatrix} F_1 \\ F_2 \\ F_3 \\ F_4 \\ F_5 \\ F_6 \end{bmatrix} \quad (2)$$

where $\mathbf{F}_x$ includes the three force components and three torque components acting at the origin *O* along the *xyz*-directions. Here, $\mathbf{F}_n$ includes the forces acting along the six wire flexures and F_n is the force component acting along the *n*th wire flexure. The dimensions *a* and *b* are defined in Fig. 5.

If the stiffness along the compliant direction (also called the parasitic stiffness) is negligible as compared to the stiffness in the stiff direction, the force component F_n will act only on the load cell attached to the *n*th wire flexure.

3.2.2 Design of a 1-DOF Load Cell Module. Six 1-DOF load cell modules were designed using a wire flexure and a 1-DOF load cell for each module. One end of the wire flexure is attached to the top plate of the FSM and the other end is attached to the load cell. The load cell is further attached to the base plate through an attachment for overload protection. Figure 6 shows the conceptual design of the module. Any force acting along the longitudinal axis of the wire flexure—tension or compression—can be measured by the attached load cell.

A safeguard was designed in order to prevent overload and buckling failure of the wire flexure. The excessive compressive load can lead to the buckling of the wire flexure. An excess load beyond the load cell measurement range can also damage the load cell. Therefore, a safety feature was implemented in order to limit the magnitude of the compressive load. The attachment collapses when the load exceeds a predetermined value. A helical spring was used to preload the attachment. The preloading can be further adjusted by an adjustment screw. If the magnitude of the compressive load acting on the wire flexure is smaller than the preloading, the reaction force is provided by the preloading. However, if the magnitude of the compressive load increases the preloading, the reaction force is provided by the spring and the spring collapses under the load. There was a small clearance provided between the top plate and the tube. The top plate comes in contact with the tube if the attachment collapses under excessive compressive load and protects the setup from further damage.

3.2.3 Dimensioning of the Wire Flexure. The wire flexure can be axially loaded both in tension and compression. The

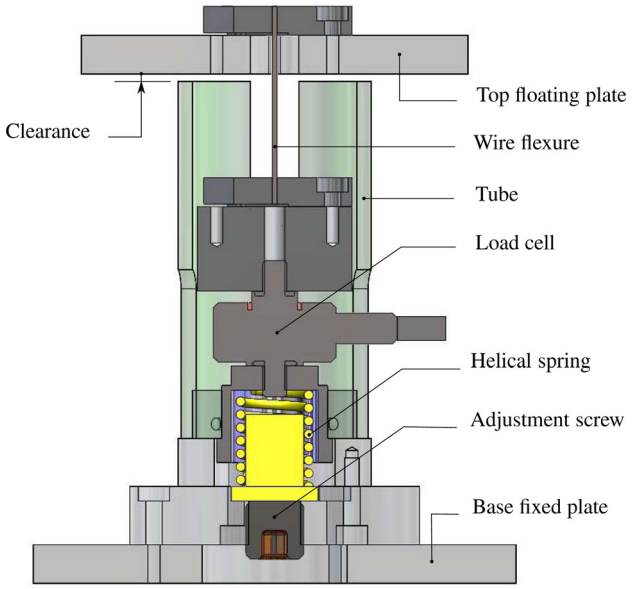

Fig. 6 Conceptual design of a 1-DOF load cell module consisting of a wire flexure, a 1-DOF load cell, and a preloading mechanism for overload protection

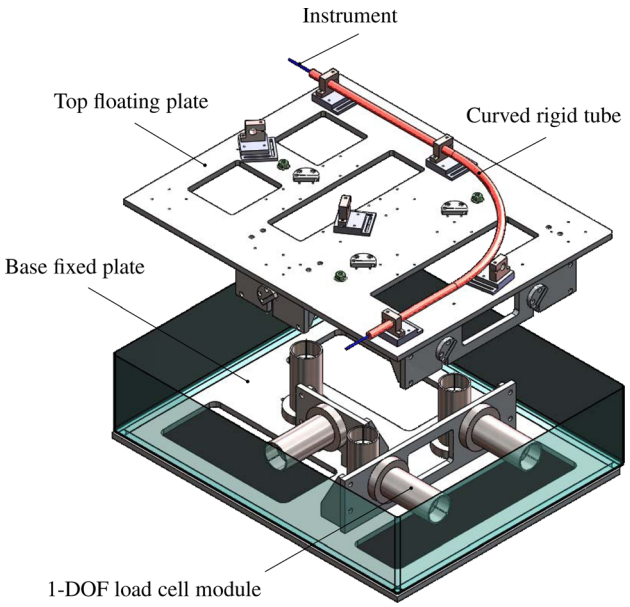

Fig. 7 Conceptual design of the FSM with six 1-DOF load cell modules. The six load cell modules are attached to the base fixed plate. The top floating plate will be attached to the ends of six wire flexures.

compressive load on the wire flexure can lead to buckling and limits the load capacity of the load cell. Therefore, the flexure should be able to support the maximum compressive load, which can be measured by the attached load cell without buckling. The critical load F_{Cr} for an undeflected wire flexure is given by

$$F_{Cr} = \frac{4\pi^2 EI}{l^2} = \frac{\pi^3}{16}\frac{Ed^4}{l^2} \tag{3}$$

where d and l are the diameter and the length of the wire flexure, respectively.

On the contrary, the wire flexure should be able to accommodate the error because of the misalignment during assembly and the manufacturing tolerances of the components. The maximum allowed deflection in the lateral direction should also include the maximum deformation possible when the other load cell module collapses because of the overload. This prevents the wire flexures from getting damaged even if the FSM is overloaded and collapsed under the load. If h is the maximum allowable deflection in the lateral direction, the maximum stress due to bending will be

$$\sigma_{max} = \frac{3Edh}{l^2} \tag{4}$$

The longitudinal stiffness k_a and the lateral stiffness k_b of the wire flexure are given by

$$k_a = \frac{EA}{l} = \frac{\pi}{4}\frac{Ed^2}{l} \tag{5}$$

$$k_b = \frac{12EI}{l^3} = \frac{3\pi}{16}\frac{Ed^4}{l^3} \tag{6}$$

From Eqs. (5) and (6), we find that the stiffness ratio is $k_a/k_b \propto (l/d)^2$. The wire flexure was designed for the maximum deflection of 1.5 mm in the compliant direction (i.e., in bending) and the maximum compressive load of 100 N without buckling. A value greater than 1000 was chosen for the stiffness ratio k_a/k_b. A higher value for the stiffness ratio ensures reduced parasitic error. Stainless steel wire 1.0 mm in diameter and 30 mm in length was chosen for the wire flexure.

3.2.4 Design Embodiment of the FSM. Six precision miniature load cells were selected based on the measurement range and the resolution. The load cell measures forces up to 100 N in both tension and compression with an accuracy of 0.15% full scale and with infinite resolution [19]. First, the six 1-DOF load cell modules were assembled, as shown in Fig. 6. All of the load cell modules were mounted on the base plate. The top plate was aligned through three fixtures and finally clamped to the six wire flexures. Figure 7 shows the design embodiment of the FSM.

3.3 Design of the T3M. The T3M was designed to measure the motion of the tip both in rotation and translation along the longitudinal axis of the instrument at the exit of the curved rigid tube. A contact with the displacement measurement modules can affect the behavior of the instrument. Since we want to study the effect of friction between the instrument and the tube, it may be very difficult to account for the output behavior. Therefore, contactless measurement is preferred. Moreover, since we are interested in displacement measurements in only two DOFs, i.e., the rotation and translation along the instrument axis, the displacements in the other four DOFs are constrained by an air bearing.

A laser displacement sensor (LDS) was chosen for the displacement measurement. The LDS uses optical triangulation as the measuring principle. A laser diode projects a visible spot of light onto the target surface. The image of the spot is captured on a high resolution CCD- or CMOS-element. The position of the target is measured by the change in the position of the reflected light on the receiver [20]. Two LDSs were used for measurement in both DOFs. A cam was designed to simultaneously facilitate measurement in both DOFs.

3.3.1 Design of a Cam. A cam is designed with two lobes, as shown in Fig. 8. The radial displacement r of a point on the cam is linearly dependent on the angular displacement θ as

$$r = r_0 + \left(\frac{r_1 - r_0}{\pi}\right)\mathrm{mod}(\theta, \pi) \tag{7}$$

where r_0 and r_1 are the radius of the base circle and outer circle enclosing the cam; $\mathrm{mod}(\theta, \pi)$ gives the modulus after dividing θ with π. Two identical lobes of 180 deg were designed. Therefore,

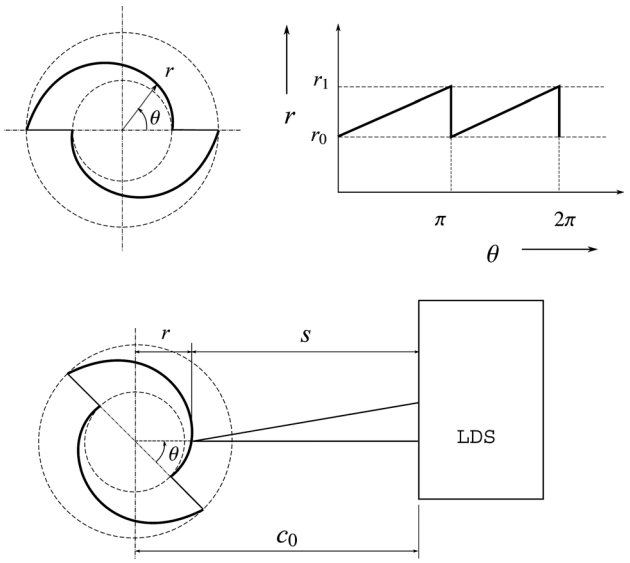

Fig. 8 Conceptual design of the cam. The angular displacement of the cam can be measured from the displacement measurement of the LDS.

after every half rotation of the cam, the plot of the radial displacement versus the angular displacement repeats, as shown in the figure. Since the distance between the cam axis and the LDS c_0 is fixed, the displacement s measured by the LDS is directly proportional to the angular displacement of the cam and is given by

$$s = (c_0 - r_0) - \left(\frac{r_1 - r_0}{\pi}\right)\mathrm{mod}(\theta, \pi) \tag{8}$$

The computer aided design (CAD) drawing of the designed cam is shown in Fig. 9. The plane surface is used to measure the displacement due to translation. The curved surface is used to measure the displacement due to rotation. An undercut is provided to ensure that the laser spot always falls on the curved surface when the cam is rotating.

3.3.2 Design Embodiment of the T3M. The conceptual design of the T3M is shown in Fig. 10. The measurement range of the LDS for the translation measurement is 50 mm with a resolution of 25 μm at 1.5 kHz [20]. The measurement range of the LDS for the rotation

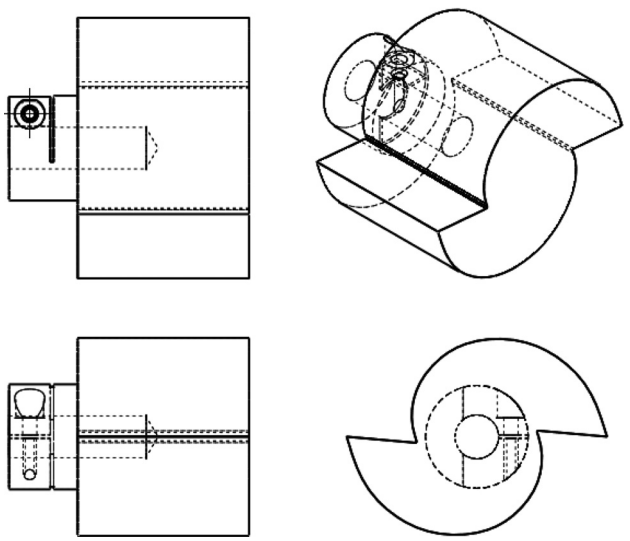

Fig. 9 CAD drawing of the cam

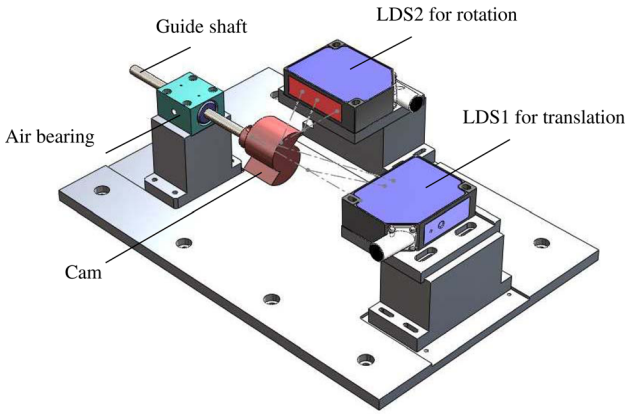

Fig. 10 Conceptual design of the T3M

measurement is 20 mm with a resolution of 10 μm at 1.5 kHz. The cam was attached to the tip of the instrument through a guide shaft, which was supported on an air bearing. The designed cam profile was obtained through wire electrical discharge machining.

3.4 Real-Time Measurement System. The experimental setup also includes the hardware and software required for real-time measurements and data logging. The measurement system was used to evaluate the setup and will be used later to characterize the behavior of the flexible instrument and to control the instrument tip motion and force.

An xPC target computer was used together with a host computer running Matlab [21]. An xPC target application was created from a Simulink model and downloaded to the target computer from the host computer via a LAN (ethernet) connection.

A multifunction I/O card was selected for data acquisition (DAQ) and control application. The DAQ card had an 8-channel fast 14-bit A/D converter with a simultaneous sample/hold circuit, 8 independent 14-bit D/A converters, 8-bit digital input port and 8-bit digital output port, 4 quadrature encoder inputs with a single-ended or differential interface, and 5 timers/counters [22].

The outputs from the six load-cells were first connected to the amplifiers and then the amplified outputs were connected to the six A/D channels. The other two A/D channels were connected to the two LDSs. The two D/A channels were connected to the two DC motor controllers. The two encoders of the DC motors were connected to the two quadrature encoder inputs. Two optical switches were used to limit the stroke of the AM translation, which were connected to the digital input port. One of the switches was used for the homing of the AM translation.

3.5 Discussion. Figure 11 shows the assembly of the experimental setup, indicating the three modules, together with the key components. The curved rigid tube was fixed on the top platform of the FSM. The flexible instrument was inserted through the tube

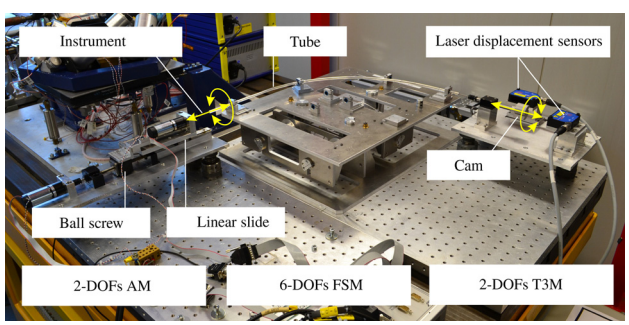

Fig. 11 Experimental setup

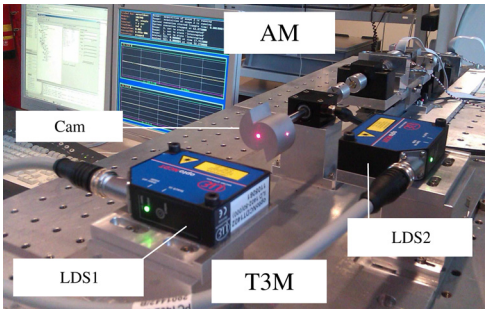

Fig. 12 The AM and the T3M were directly connected for the design evaluation

and the two ends of the instrument were attached to the AM and the T3M for the actuation and measurement of the two DOFs, respectively. The AM and the T3M were aligned to the entry and exit of the tube.

4 Design Evaluation

Table 1 shows the design specifications of the three modules—AM, FSM, and T3M. The designed setup has to be evaluated for the given specifications. First, the AM and the T3M were directly connected through a coupling for a combined evaluation, as shown in Fig. 12. Next, the FSM was separately evaluated and characterized.

4.1 Evaluation of the AM and the T3M. We wanted to evaluate the following parameters of the AM and the T3M:

1. Translation of the AM
   (a) resolution
   (b) error due to gear backlash
2. Rotation of the AM
   (a) resolution
   (b) error due to gear backlash
3. Translation measurement of the T3M
   (a) resolution
   (b) sensitivity of the LDS1
   (c) error due to the nonlinearity of the LDS1
4. Rotation measurement of the T3M
   (a) resolution
   (b) sensitivity of the LDS2
   (c) error due to the nonlinearity of the LDS2.

The measurements of these parameters were performed through several experiments, which are explained in the following sections.

4.1.1 Resolution of the AM. The translation axis of the AM has an encoder of $N_p = 1000$ pulses per revolution and the DAQ acquires the signal through a quadrature encoder input. Including the pitch of the ball screw p and the gear ratio n_g, the resolution based on the encoder resolution is, therefore, given by

$$\Delta x_{\text{res}} = \frac{p}{4N_p n_g} \tag{9}$$

For $p = 2$ mm per revolution and $n_g = 4.38$, the resolution, thus calculated, is 0.1 μm. The rotation axis of the AM also has the encoder of 1000 pulses per revolution and the DAQ acquires the signal through the quadrature encoder input. The gear ratio is 19.22. Therefore, the resolution based on the encoder resolution is 0.005 deg.

However, the actual resolution is always marred by the friction in the system. The resolution of the AM in translation and rotation, as mentioned in Table 1, will be sufficient for the characterization of the flexible instrument and the validation experiments.

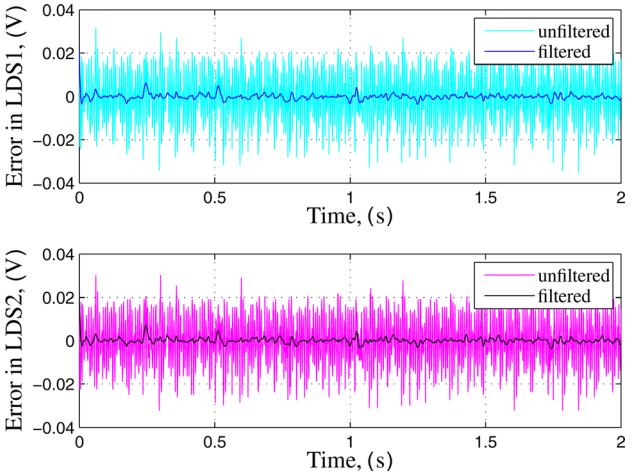

Fig. 13 Static error measurement of the LDS1 and LDS2

4.1.2 Resolution of the T3M. The resolution of the T3M for the translation and rotation measurements were obtained from static measurements of the LDS1 and LDS2. The static measurements give an indication of the level of sensor noise and the effect of the selected bandwidth on the resolution. A sample rate of 1 kHz was used for the measurement. Figure 13 shows the static error measurement of the LDS1 and LDS2 when the cam was in the measurement range of both sensors. A rather noisy signal was observed in both cases. The power spectral density of the data showed high power in the frequency range of 100–150 Hz. In order to reduce the sensor noise, a 2nd order low-pass digital Butterworth filter was designed with a cut-off frequency of 45 Hz. The data were filtered off-line, forward and backward in time, to achieve zero-phase digital filtering [23]. The static error was calculated by subtracting the mean value from the filtered data. The plots of the static error after filtering were also included in Fig. 13 for both sensors. We observed that the sensor noise was considerably reduced after filtering.

Static measurements were taken for the different positions in the measurement range to determine if the error is same over the measurement range. Three different positions along the translation axis were considered—the start, middle, and end of the measurement range. The output voltage from the LDS was measured and the root mean square (RMS) value of the error was calculated from the standard deviation. The RMS values were calculated for both the unfiltered and filtered data for both the LDS1 and LDS2. In addition, for the LDS2 the static measurements were taken at three different positions in the measurement range. The sensitivity of each LDS was calculated from the change in the output voltage corresponding to the change in the input displacement (as will be explained later in Secs. 4.1.3 and 4.1.4). After dividing with the sensitivity of the LDS, we obtained the error in the displacement measurement. Table 3 shows the result of the static error measurement taken from both of the sensors. The error was reduced

Table 3 Static error measurement of the LDS

	Unfiltered		Filtered	
LDS1	RMS value (mV)	Error	RMS value (mV)	Error
Start	8	0.10 mm	0.9	11 μm
Middle	11	0.14 mm	1.2	15 μm
End	11.5	0.14 mm	1.1	14 μm
LDS2				
Start	10.6	1.0 deg	1.4	0.13 deg
Middle	10.4	0.9 deg	1.2	0.11 deg
End	10.5	1.0 deg	1.4	0.13 deg

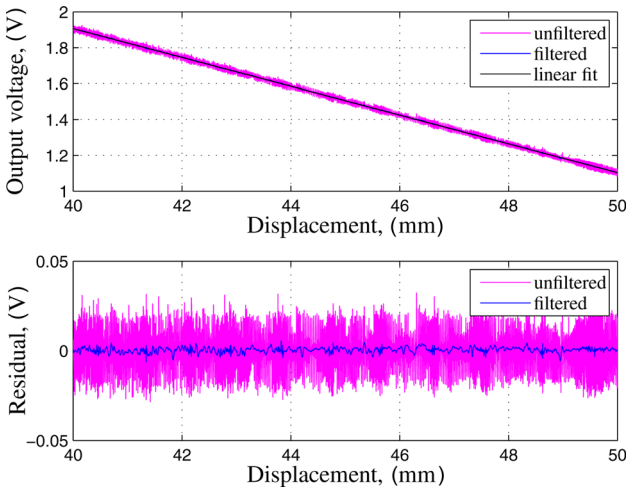

Fig. 14 Output voltage from the LDS1 for the translation measurement of the cam

approximately nine times after the filtering. The errors in the translation and rotation measurement are about 15 μm and 0.15 deg, respectively. Therefore, the resolution will also be of the same order. However, the resolution can be better or worse, depending on the bandwidth chosen. For our application, a cut-off frequency of 45 Hz will be sufficient to capture the characteristic behavior of the flexible instrument.

4.1.3 Sensitivity Measurement of the LDS1. For the sensitivity measurement of the LDS1, the output voltage from the LDS1 was obtained for the input displacement of the AM translation. The input displacement was obtained from the encoder reading. Figure 14 shows the plot of the output voltage from the LDS1 for the translation measurement. A linear fit was applied to the data. The slope of the linear fit gives the sensitivity value, which was 0.0803 V/mm.

The residual is calculated by subtracting the fitted data from the measurement data. The residual plot is also shown in Fig. 14. The error was calculated from the RMS value of the residuals. The RMS value of 11 mV was obtained, which was of the same order as the sensor noise. The data were filtered off-line using the zero-phase digital filtering, as explained in Sec. 4.1.2. The plot of the residuals of the filtered data from the linear fit was also shown in the figure. The error, thus obtained, was 1.3 mV. The error was reduced more than eight times after the filtering. The error in the translation measurement due to the nonlinearity of the sensor, obtained by dividing with the sensitivity of the LDS1, was 16 μm.

4.1.4 Sensitivity Measurement of the LDS2. Similarly, for the sensitivity measurement of the LDS2, the output voltage from the sensor was obtained for the input displacement of the AM rotation. Figure 15 shows the plot of the voltage output from the

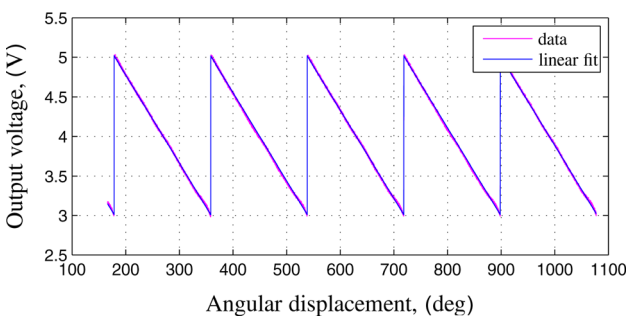

Fig. 15 Output voltage from the LDS2 for continuous rotation of the cam

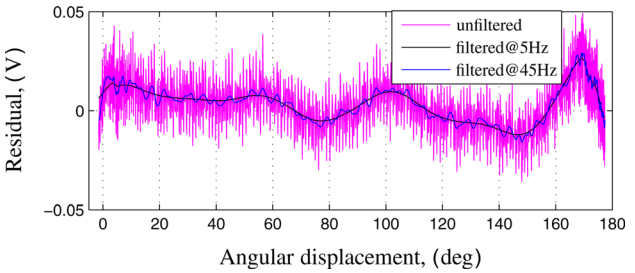

Fig. 16 Residual plot of the LDS measurement for rotation after a linear fit

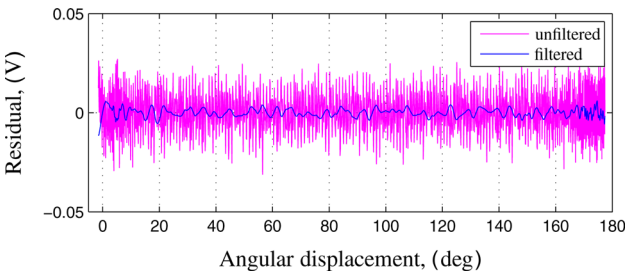

Fig. 17 Residual plot of the LDS measurement for rotation after subtracting the filtered data corresponding to the cam profile

LDS2 for the rotation measurement. A linear fit was obtained for every 180 deg rotation of the cam, assuming the two lobes of the cam were identical. The sensitivity of the LDS2, thus obtained from the slope of the plot, was 0.0111 V/deg.

Figure 16 shows the residual plot of the LDS2 measurement from the linear fit. The data were filtered off-line by applying the zero-phase digital filtering, as explained in Sec. 4.1.2, at a cut-off frequency of 5 Hz to obtain the shape of the cam profile. The data were filtered for a cut-off frequency of 45 Hz also for the error measurement. The figure also shows the plots of the residuals of the filtered data from the linear fit. The RMS value of the residuals gives the error because of the nonlinearity of the cam. The RMS value of the error, thus obtained, was 9.2 mV. The corresponding error in the angle measurement was 0.84 deg. The linearity of the cam is, therefore, 0.5%. However, the error in the measurement can be further improved by using the look-up table for the cam.

Figure 17 shows the residual plots of the unfiltered and filtered data (at 45 Hz) from the filtered data (at 5 Hz) corresponding to the cam profile. These residual plots provide the error if the cam profile is taken into consideration. The RMS values for the unfiltered and filtered data were 10.6 mV and 2.3 mV, respectively, and the corresponding errors in the angular measurement are 0.96 deg and 0.21 deg, respectively.

4.1.5 Backlash Measurement in the AM Translation. For the backlash measurement in the translation axis of the AM, the displacement measurement of the LDS1 was compared with the encoder reading corresponding to the translation, while the AM was moving in both directions along the translation axis. The input motion was given by rotating the coupling, which connects the gear shaft to the ball screw. As the coupling was rotated, the ball screw was already moving, but the motor encoder was not moving because of the clearance in the gear box. Figure 18 shows the plot of the unfiltered and filtered data. The data were filtered using the zero-phase digital filtering, as explained in Sec. 4.1.2. A backlash of 0.2 mm was observed in the translation axis.

4.1.6 Backlash Measurement in the AM Rotation. Similarly, for the backlash measurement in the rotation axis of the AM, the cam was rotated in both directions by rotating the coupling which connects the gear shaft with the T3M (as shown in Fig. 12). The

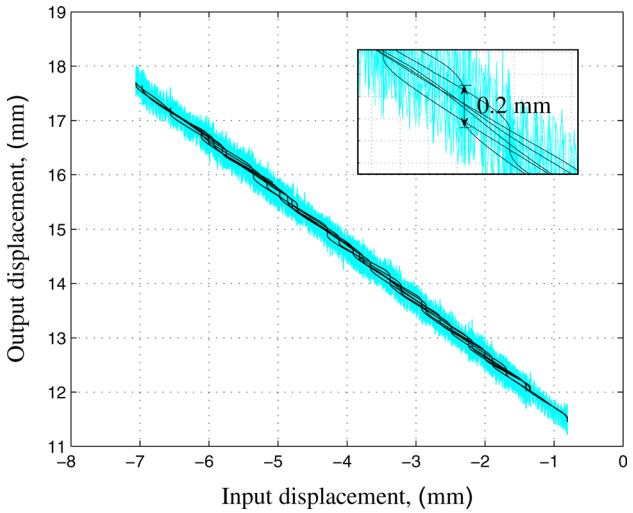

Fig. 18 Output displacement measured by the LDS1 compared with the input displacement measured from the encoder, showing the gear backlash in translation

displacement measurement of the LDS2 was compared with the encoder measurement along the rotation axis. Figure 19 shows the plot of the unfiltered and filtered data. The data were filtered using the zero-phase digital filtering, as explained in Sec. 4.1.2. The backlash of 1.0 deg was observed due to the clearance in the gear box.

4.2 Evaluation of the FSM. The FSM was designed to measure the external forces and moments acting on the top floating plate. The designed module was calibrated by applying forces at known locations. If an external force and moment $\mathbf{F}_{\text{ext}}$ is applied at point P on the floating platform, the load cells attached to the base of six wire flexures will be loaded. Figure 20 illustrates the loading configuration. The equivalent force $\mathbf{F}_x$ acting at the origin O can be expressed as

$$\mathbf{F}_x = B\mathbf{F}_{\text{ext}}$$

or

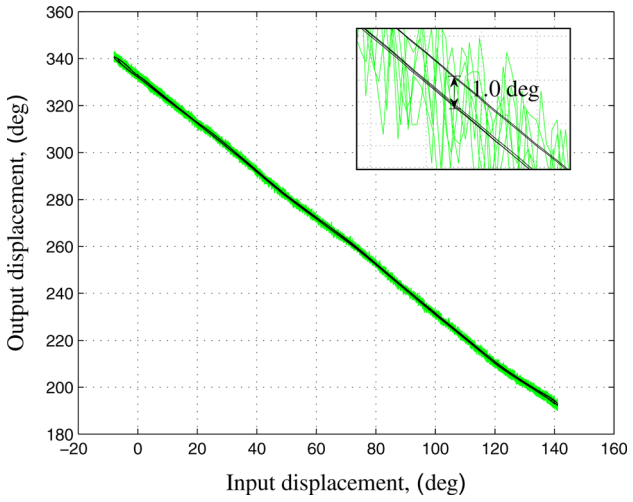

Fig. 19 Output displacement measured by the LDS2 compared with the input displacement measured from the encoder, showing the gear backlash in rotation

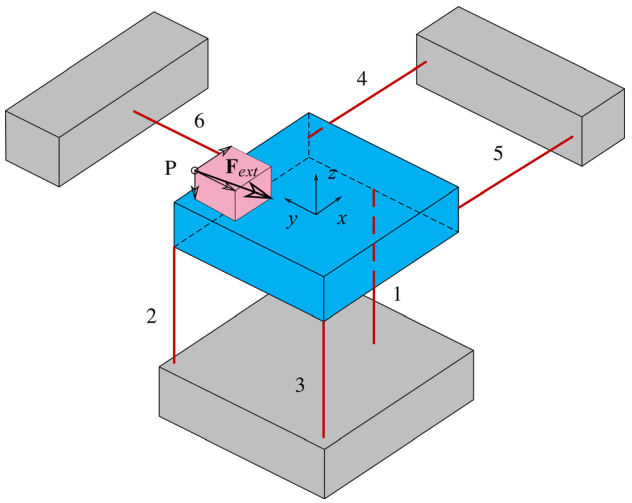

Fig. 20 Loading configuration showing the external load applied on the top floating plate of the FSM at point P; $\mathbf{F}_{\text{ext}}$ includes the external forces and moments

$$\begin{bmatrix} F_x \\ F_y \\ F_z \\ M_x \\ M_y \\ M_z \end{bmatrix} = \begin{bmatrix} 1 & 0 & 0 & 0 & 0 & 0 \\ 0 & 1 & 0 & 0 & 0 & 0 \\ 0 & 0 & 1 & 0 & 0 & 0 \\ 0 & -z & y & 1 & 0 & 0 \\ z & 0 & -x & 0 & 1 & 0 \\ -y & x & 0 & 0 & 0 & 1 \end{bmatrix} \begin{bmatrix} F'_x \\ F'_y \\ F'_z \\ M'_x \\ M'_y \\ M'_z \end{bmatrix} \tag{10}$$

where (x,y,z) are the coordinates of the point P with respect to the origin. Here, F'_x, F'_y, and F'_z are the forces and M'_x, M'_y, and M'_z are the moments acting at point P along the xyz-directions, respectively.

Here, $\mathbf{F}_x$ can be further transformed into a force vector $\mathbf{F}_n$, consisting of six force components along the wire flexures, as expressed in Eq. (2).

If S is the sensitivity matrix of the load cells of the FSM, the voltage output of the load cells $\mathbf{V}_n$ is related to the force vector $\mathbf{F}_n$ as

$$\mathbf{V}_n = S\mathbf{F}_n$$

or

$$\begin{bmatrix} V_1 \\ V_2 \\ V_3 \\ V_4 \\ V_5 \\ V_6 \end{bmatrix} = \begin{bmatrix} s_{11} & s_{12} & s_{13} & s_{14} & s_{15} & s_{16} \\ s_{21} & s_{22} & s_{23} & s_{24} & s_{25} & s_{26} \\ s_{31} & s_{32} & s_{33} & s_{34} & s_{35} & s_{36} \\ s_{41} & s_{42} & s_{43} & s_{44} & s_{45} & s_{46} \\ s_{51} & s_{52} & s_{53} & s_{54} & s_{55} & s_{56} \\ s_{61} & s_{62} & s_{63} & s_{64} & s_{65} & s_{66} \end{bmatrix} \begin{bmatrix} F_1 \\ F_2 \\ F_3 \\ F_4 \\ F_5 \\ F_6 \end{bmatrix} \tag{11}$$

where s_{ij} is the sensitivity of the ith load cell because of the jth component of the force $\mathbf{F}_n$. If the wire flexures have only longitudinal stiffness k_a and negligible lateral stiffness k_b, the force component F_n will directly act on the nth load cell. Therefore, for the larger ratio of stiffnesses k_a/k_b, the sensitivity matrix S will be a diagonal matrix and the diagonal terms will be the individual sensitivities of the load cells. However, because of the nonzero lateral stiffness (also called the parasitic stiffness) of the wire flexures, there will be resultant forces acting on the other load cells arising from the force acting along one of the load cells. This results in nonzero off diagonal terms. The inaccuracies in the fabrication of

Table 4 Static measurement of the load cells

Load cells		1	2	3	4	5	6
Unfiltered	RMS value (mV)	3.3	2.9	3.1	2.9	2.8	2.9
	Error (mN)	15.3	13.4	14.3	13.7	13.7	13.7
Filtered (at 45 Hz)	RMS value (mV)	1.9	0.9	1.0	1.2	0.9	0.8
	Error (mN)	8.8	4.2	4.6	5.9	4.3	3.8

the mechanical components and their assembly will also contribute to nonzero off diagonal terms.

The evaluation of the FSM requires the calculation of the following parameters:

(1) resolution of the load cells
(2) Sensitivity of the load cells and the FSM
(3) error measurement of the FSM

The measurements of these parameters were performed through several experiments, which are explained in the following sections.

4.2.1 Resolution of the Load Cells. Static measurements were taken from the load cells in order to obtain the sensor noise and the resolution. The output voltage from the six load cells was measured without an external load applied on the FSM. The loading on the load cells was from the weight of the top floating platform and the load due to the initial deflections along the compliant directions of the wire flexures.

Table 4 shows the static error measurement of the load cells. The RMS value of the error was calculated for each load cell for both the unfiltered and filtered data. The filtered data were obtained by the zero-phase digital filtering, as explained in Sec. 4.1.2, for a cut-off frequency of 45 Hz. The corresponding error in the force measurement was obtained by dividing with the individual sensitivity of the load cell, which will be explained later in Sec. 4.2.2. The error in the force measurement, thus calculated, was of the order of 9 mN after filtering. Therefore, the resolution of the load cells is 9 mN at 45 Hz.

4.2.2 Sensitivity of the Load Cells and the FSM. For the sensitivity measurement of the load cells and the FSM, the output voltage of the load cells were measured by applying different loads at various locations along different directions. For a set of N measurements using Eq. (11), the output voltage and the force components along the load cells for different applied external loads can be written as

$$\left[\mathbf{V}_{n,1}\mathbf{V}_{n,2}\cdots\mathbf{V}_{n,N}\right] = S\left[\mathbf{F}_{n,1}\mathbf{F}_{n,2}\cdots\mathbf{F}_{n,N}\right]$$

or

$$[V_{nN}] = S[F_{nN}] \tag{12}$$

where $\mathbf{V}_{n,j}$ and $\mathbf{F}_{n,j}$ are the output voltage from the load cells $\mathbf{V}_n$ and the force components $\mathbf{F}_n$ for the jth measurement. Here, $\mathbf{F}_n$ is calculated for each applied external load $\mathbf{F}_{\text{ext}}$. Using Eqs. (2) and (10), we have

$$\mathbf{F}_n = A^{-1}B\mathbf{F}_{\text{ext}} \tag{13}$$

The individual sensitivities of the load cells S_i were directly obtained by plotting the output voltage V_{iN} with respect to the load F_{iN} acting along the ith load cell. Figure 21 shows the plot of the output voltage of the load cells. The sensitivities of the individual load cells were obtained from the slopes of the linear fit and summarized in Table 5. The off diagonal elements cannot be obtained by this method.

Alternatively, the full sensitivity matrix S of the load cells of the FSM can be calculated from Eq. (12) using the pseudoinverse as

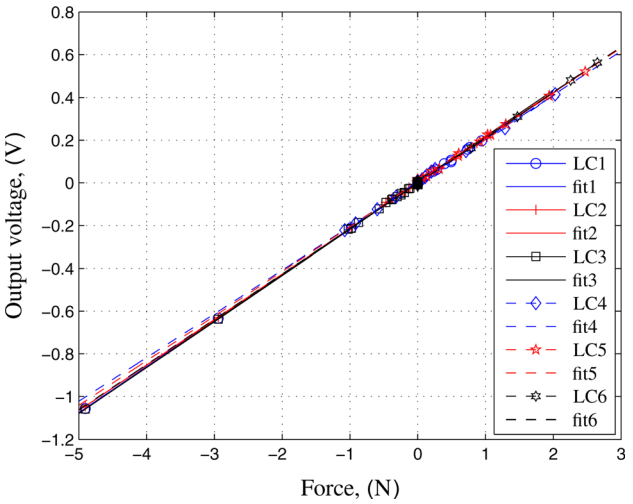

Fig. 21 Output voltage of the load cells for the forces acting along the load cells

Table 5 Individual sensitivity of the load cells

	S_1	S_2	S_3	S_4	S_5	S_6
Sensitivity (V/N)	0.215	0.213	0.216	0.205	0.209	0.212

$$S = \left[\mathbf{V}_{n,1}\mathbf{V}_{n,2}\cdots\mathbf{V}_{n,N}\right]\left[\mathbf{F}_{n,1}\mathbf{F}_{n,2}\cdots\mathbf{F}_{n,N}\right]^{+}$$

or

$$S = [V_{nN}][F_{nN}]^{+} \tag{14}$$

where $[F_{nN}]^{+}$ is the pseudoinverse of the matrix. The sensitivity matrix, thus obtained, is

$$S = \begin{bmatrix} 0.2152 & 0.0010 & -0.0006 & -0.0008 & -0.0003 & 0.0004 \\ 0.0008 & 0.2135 & 0.0009 & 0.0010 & 0.0033 & -0.0012 \\ -0.0001 & -0.0003 & 0.2162 & 0.0004 & 0.0026 & 0.0007 \\ -0.0018 & 0.0008 & 0.0010 & 0.2035 & 0.0068 & -0.0039 \\ 0.0001 & 0.0003 & -0.0036 & 0.0039 & 0.2108 & -0.0005 \\ 0.0015 & -0.0005 & 0.0017 & -0.0086 & 0.0061 & 0.2067 \end{bmatrix} \tag{15}$$

The diagonal and off diagonal elements can be simultaneously obtained. We also observed that the diagonal elements are at least 24 times higher than the off diagonal elements. It was also observed that the diagonal elements are almost identical to the individual sensitivities of the load cells.

4.2.3 Error Measurement of the FSM. The forces acting on the FSM are measured in the xyz-coordinates. Therefore, the error in measurement should be expressed in terms of three forces and three moments along the xyz-coordinates. The estimated force $\widehat{\mathbf{F}}_x$ can be calculated from the output voltage readings of the load cells $\mathbf{V}_n$ using Eqs. (2) and (11) as

$$\widehat{\mathbf{F}}_x = AS^{-1}\mathbf{V}_n \tag{16}$$

where $\mathbf{F}_x$ can be directly obtained from the applied external load $\mathbf{F}_{\text{ext}}$ using Eq. (10). The error can be calculated from $\mathbf{F}_x$ and $\widehat{\mathbf{F}}_x$.

The relative errors in the force and moment measurements were calculated for a new set of experiments where known loads were applied on the top floating plate of the FSM. Figure 22 shows the

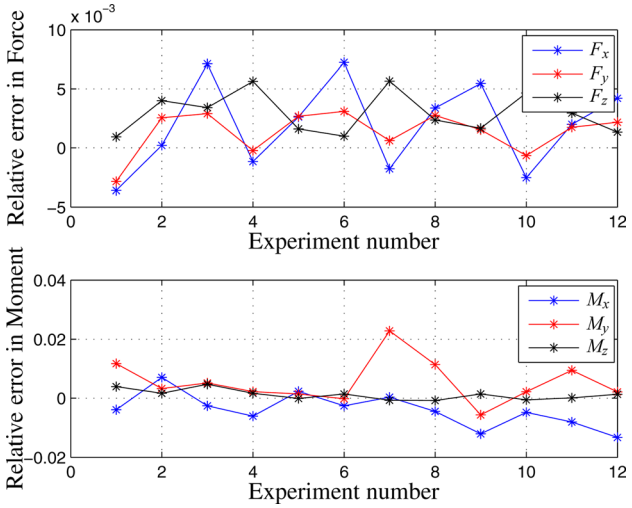

Fig. 22 Relative error in the force and moment measurement

plot of relative error in the force and moment measurements. The error obtained in the force and moment measurements are less than 0.8% and 2.5%, respectively.

5 Discussion

The AM has a translation resolution of 0.1 μm and a rotation resolution of 0.005 deg based on the encoder resolution. However, the actual resolution is always marred by the friction in the system. However, the resolution of the AM at least exceeds the resolution of the T3M, which is on the order of 15 μm in translation and 0.15 deg in rotation. This will be sufficient for the characterization of the flexible instrument and the validation experiments. The largest errors of the AM are because of the gear backlash. The backlash observed in the translation and rotation is 0.2 mm and 1.0 deg, respectively. The motion hysteresis observed in the simulation of flexible instruments were on the order of 2 mm in translation [7,9]. The motion hysteresis in rotation is expected to be on the order of 10 deg. However, if required, the gear can be replaced or preloaded. The AM can achieve slow speeds on the order of 0.2 mm/s in translation and 0.1 rev/s in rotation, which can be useful for the study of stick-slip behavior of the instrument. The AM can achieve a higher speed of 30 mm/s in translation and 4 rev/s in rotation, which can be used to generate a combination of the translation and rotation motions.

We used a low pass filter with a cut-off frequency of 45 Hz for improving the resolution of the T3M. This enables filtering any noise due to the power supply of 50 Hz. At the same time, it is high enough to perform dynamic measurements. However, the stick-slip behavior of flexible instruments due to friction may require higher bandwidth. The error in the rotation measurement due to the nonlinearity of the cam is on the order of 1.0 deg. However, the error was reduced to 0.2 deg if the cam profile was taken into consideration. The specifications of the T3M are comparable to the design specifications.

The load cells of the FSM have a measurement range of 50 N with a resolution of 9 mN at 45 Hz. The error in the measurements of the force and moment are less than 0.8% and 2.5%, respectively. These values allow for the accurate measurement of the forces that a flexible instrument exerts on the tube.

The designed experimental setup is used to validate the simulation results from the flexible multibody model of a flexible instrument inside a curved rigid tube. The achieved specifications of the three modules—AM, FSM, and T3M—enabled us to provide actuation in translation and rotation along the longitudinal axis of the instrument at the proximal end, to measure the interaction forces, and to measure the translation and rotation of the distal end of the instrument. However, the details of the experiments are beyond the scope of this paper and can be found in Ref. [24].

6 Conclusion

We designed the experimental setup based on the design requirements necessary to validate the flexible multibody model and to characterize the flexible instruments inside an endoscope. The actuation module provides the actuation in the axial and twist directions from the proximal end of the flexible instrument. Although there is a backlash of 0.2 mm and 1.0 deg in the module, the motion hysteresis in the case of a flexible instrument is at least 10 times higher than the error due to backlash. The tip motion measurement module achieves contactless measurement of the distal end motion in the axial and twist directions via an air bearing guided cam. Off-line filtering helps to improve the resolution to 15 μm and 0.15 deg. The force sensing module measures the force and moment exerted by the flexible instrument on the curved tube, which is fixed to the floating platform. The force resolution of 9 mN and the force and moment error of 0.8% and 2.5%, respectively, are within the specifications. The three modules of the setup conform to the design objectives. The experimental setup is used for the validation of the developed model of the flexible instrument inside a curved rigid tube.

Acknowledgment

The authors would like to thank Mr. L. Tiemersma for his contribution to the realization of the setup, and Dr. Johannes van Dijk for his help in xPC and control.

This research is funded by the TeleFLEX Project No. PID07038, by the Dutch Department of Economic Affairs, Agriculture and Innovation and the Province of Overijssel within the PIDON initiative.

References

[1] Gomes, P., 2011, "Surgical Robotics: Reviewing the Past, Analysing the Present, Imagining the Future," Rob. Comput.-Integr. Manufact., **27**(2), pp. 261–266.
[2] Lanfranco, A. R., Castellanos, A. E., Desai, J. P., and Meyers, W. C., 2004, "Robotic Surgery: A Current Perspective," Ann. Surg., **239**(1), pp. 14–21.
[3] Camarillo, D. B., Krummel, T. M., and Salisbury, J. K., 2004, "Robotic Technology in Surgery: Past, Present, and Future," Am. J. Surg., **188**(1), pp. 2–15.
[4] Swanström, L. L., Khajanchee, Y., and Abbas, M. A., 2008, "Natural Orifice Transluminal Endoscopic Surgery: The Future of Gastrointestinal Surgery," The Permanente J., **12**(2), pp. 42–47.
[5] Chamberlain, R. and Sakpal, S., 2009, "A Comprehensive Review of Single-Incision Laparoscopic Surgery (SILS) and Natural Orifice Transluminal Endoscopic Surgery (NOTES) Techniques for Cholecystectomy," J. Gastrointest. Surg., **13**(9), pp. 1733–1740.
[6] Olympus America Inc., 2013, "Olympus EndoTherapy," http://www.olympusamerica.com/presspass/press_pass_cut/msg_pressone.asp
[7] Khatait, J. P., Krijnen, M., Meijaard, J. P., Aarts, R. G. K. M., Brouwer, D. M., and Herder, J. L., 2011, "Modelling and Simulation of a Flexible Endoscopic Surgical Instrument in a Tube," ASME 2011 International Mechanical Engineering Congress and Exposition (IMECE2011), Denver, CO, November 11–17, Vol. 2, American Society of Mechanical Engineers (ASME), New York, ASME Paper No. IMECE2011-65189, pp. 557–566.
[8] Khatait, J. P., Brouwer, D. M., Meijaard, J. P., Aarts, R. G. K. M., and Herder, J. L., 2012, "3-D Multibody Modeling of a Flexible Surgical Instrument Inside an Endoscope," ASME 2012 International Mechanical Engineering Congress and Exposition, Houston, TX, November 9–15, American Society of Mechanical Engineers (ASME), New York.
[9] Khatait, J. P., Brouwer, D. M., Aarts, R. G. K. M., and Herder, J. L., 2013, "Modeling of a Flexible Instrument to Study Its Sliding Behavior Inside a Curved Endoscope," ASME J. Comput. Nonlinear Dyn., **8**(3), p. 031002.
[10] Slocum, A. H., 1992, *Precision Machine Design*, Society of Manufacturing Engineers, Dearborn, MI.
[11] Schellekens, P., Rosielle, N., Vermeulen, H., Vermeulen, M., Wetzels, S., and Pril, W., 1998, "Design for Precision: Current Status and Trends," CIRP Ann., **47**(2), pp. 557–586.
[12] Okamura, A. M., Simone, C., and O'Leary, M. D., 2004, "Force Modeling for Needle Insertion Into Soft Tissue," IEEE Trans. Biomed. Eng., **51**, pp. 1707–1716.
[13] Trejos, A. L., Patel, R. V., and Naish, M. D., 2010, "Force Sensing and Its Application in Minimally Invasive Surgery and Therapy: A Survey," Proc. Inst. Mech. Eng., Part C: J. Mech. Eng. Sci., **224**(7), pp. 1435–1454.

[14] Soemers, H. M. J. R., 2010, *Design Principles for Precision Mechanisms*, T-Point, Enschede, The Netherlands.
[15] Blanding, D. L., 1999, *Exact Constraint: Machine Design Using Kinematic Principles*, American Society of Mechanical Engineers (ASME), New York.
[16] Aarts, R. G. K. M., Meijaard, J. P., and Jonker, J. B., 2012, "Flexible Multibody Modelling for Exact Constraint Design of Compliant Mechanisms," Multibody Syst. Dyn., **27**(1), pp. 119–133.
[17] MISUMI Europa GmbH, 2010, "Mechanical Components for Assembly Automation," Schwalbach, Germany.
[18] Maxon motor ag, 2010, "High Precision Drives and Systems," Sachseln, Switzerland.
[19] Honeywell Sensing and Control, 2010, "Miniature Load Cell." Columbus, OH.
[20] Micro-Epsilon Messtechnik, 2010, "Laser Sensors for Displacement and Position," Ortenburg, Germany.
[21] The MathWorks, Inc., 2010, "xPC Target™ User's Guide." Natick, MA.
[22] HUMUSOFT®, 2010, "MF624, Multifunction I/O Card, User's Manual," Czech Republic.
[23] The MathWorks, Inc., 2010, "Signal Processing Toolbox™ User's Guide," Natick, MA.
[24] Khatait, J. P., 2013, "Motion and Force Transmission of a Flexible Instrument Inside a Curved Endoscope," Ph.D. thesis, University of Twente, Enschede, The Netherlands.